



Wheat Straw Cellulose Amorphous Porous Carbon Used As Anode Material for a Lithium-Ion Battery

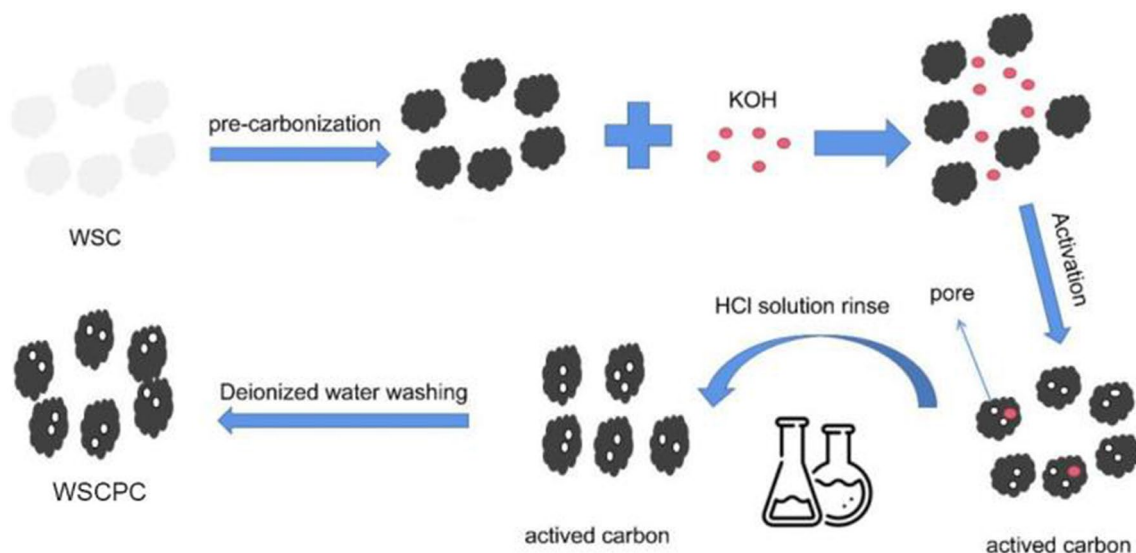
Kaifeng Yu¹ · Baoying Wang¹ · Peiming Bai^{1,2} · Ce Liang¹ · Wenming Jin^{1,2}

Received: 10 June 2021 / Accepted: 13 August 2021 / Published online: 3 September 2021
© The Minerals, Metals & Materials Society 2021

Abstract

Biomass-derived carbons are used efficiently in energy storage systems due to low cost, spacious distribution, and porous structure. Herein, we propose an uncomplicated method to prepare wheat straw cellulose porous carbon (WSCPC) using wheat straw cellulose as the carbon source and potassium hydroxide (KOH) as the activation agent. A series of characterizations are performed on six samples treated with different amounts of activator. Scanning electron microscopy (SEM) and transmission electron microscopy (TEM) confirm that WSCPC-4 (4:1 mass ratio of activator to carbon) has an abundant pore structure over the surface, with a high surface area of $628 \text{ m}^2 \text{ g}^{-1}$. Furthermore, a reversible capacity of 1420 mAh g^{-1} at 0.2 C is obtained after 100 cycles. These results indicate that wheat straw porous carbon provides an effective method for designing high specific capacity electrode materials.

Graphic Abstract



Keywords Wheat straw · cellulose · porous carbon · anode · lithium-ion battery

✉ Wenming Jin
jwmjlu@126.com

Ce Liang
liangce@jlu.edu.cn

¹ Key Laboratory of automobile Materials, Ministry of Education, and College of Materials Science and Engineering, Jilin University, Changchun 130025, China
² Roll Forging Research Institute, Jilin University, Changchun 130025, Jilin, China

Introduction

New energy vehicles and portable smart communication devices are developing rapidly.¹ Hence, the demand for rechargeable batteries with high energy density have been increasing rapidly. Among the available rechargeable energy storage systems, lithium-ion batteries (LiBs) have become the most promising potential energy storage power source due to their high working voltage, high energy density, and low self-discharge rate.^{2,3} At present, graphite, the commercial anode material for lithium-ion batteries, has a low theoretical specific capacity (372 mAh g⁻¹) and poor rate performance that cannot meet the growing application requirements.⁴⁻⁶ In addition, with the decrease of natural resources, the future research direction of anode materials for lithium-ion batteries will shift to high cycle performance and low cost.⁷ In recent years, high-performance lithium-ion batteries have attracted research attention due to the large-scale expansion of the electric vehicle field.

A renewable energy source, biomass-derived carbon is widely used as anode material for LiIB due to its low cost, rapid renewability, and environmental friendliness. At the same time, it has also been applied across disciplines.⁸⁻¹⁴ Biomass carbon has a wide range of sources, including hemp straw, lignin, corn stalk, sweet potato peel, melon seed peel, pine nut peel, banana peel, jute straw, wheat straw, buckwheat husk, etc.¹⁵⁻²³ Among various carbon materials, porous carbon has excellent electrochemical properties. During the charge transfer reaction process, the porous structure promotes the electrode/electrolyte contact interface, which helps to provide a shorter lithium-ion diffusion path for lithium ion migration.²⁴⁻²⁸ Therefore, biomass-derived porous carbon materials produce high-performance anode materials, which has been reported in many studies. Nahm's team²⁹ synthesized activated carbon by KOH and ZnCl₂ from banana fibre by a pyrolysis treatment. Cao et al.³⁰ prepared hierarchical porous nitrogen-doped carbon (HPNC) nanosheets via simultaneous activation and graphitization of biomass-derived natural silk. Sekars et al.³¹ used waste green tea powder to synthesize nanosheets through certain steps, and after activation by potassium hydroxide, they showed a polymerized mesoporous interconnected network nanosheet.

Wheat straw has many applications, including fuel, bio-composite materials, livestock feed, building materials, papermaking, etc.³²⁻³⁴ However, most wheat straw is burned directly in the field, causing serious environmental pollution. Consequently, the green and efficient application of wheat straw is significantly needed. It is reported that wheat straw has a natural plant fiber structure, which can provide activated carbon for the preparation of supercapacitors. It can also be converted into porous carbon by an activator to become a high-capacity lithium-ion battery anode material.³⁵⁻³⁷

In the present work, to obtain advanced carbon anode materials with excellent conductivity and abundant Li⁺ storage sites, we extracted cellulose from wheat straw to prepare porous amorphous carbon with a KOH activation agent. Benefiting from the rich porous structure, the as-prepared WSCPC exhibits excellent electrochemical activities and rate performance. Among the as-obtained samples, WSCPC-4 showed a high specific capacity of 1420 mAh g⁻¹ at a current density of 0.2 C after 100 cycles and also excellent rate performance. Biomass carbon material has sufficient characteristics in terms of structure and electrochemistry so that it has more advantages in practical applications.

Experiment

Material Preparation

The preparation process of wheat straw cellulose is shown in Fig. 1. First, the wheat straw was pulverized into powder, then washed by deionized water to remove impurities and dried in an oven at 70°C. Two grams of powder was dispersed into 30 mL of 2 mol L⁻¹ NaOH solution and the mixture was poured into a Teflon-lined stainless steel autoclave. The lignin of the wheat straw is removed under 180°C conditions for 12 h. Subsequently, the black precipitates were taken out and washed alternately with alcohol aqueous solution to neutrality and dried in an oven at 70°C. Next, the residues were immersed in 4 wt.% H₂SO₄ solution and stirred in a constant temperature water bath at 95°C for 3 h to remove hemicellulose and impurity metal ions. Then, acid-treated powder was washed with water to until pH close to 7 and dried in a constant temperature oven. Finally, the white wheat straw cellulose was obtained (WSC).

Preparation of WSCPC. In the first step, the wheat straw cellulose was put into a muffle furnace and calcined at 300°C for 3 h to obtain precursor. Then, KOH was mixed with the precursor in weight ratios of 0:1, 1:1, 2:1, 3:1, 4:1, 5:1, respectively, thoroughly ground, and then dispersed into deionized water. After evenly stirring for 3 h, the mixture was transferred to an oven at 65°C to remove the water content. Afterward, it was put into a tube furnace to pyrolyze under Ar atmosphere at 600°C for 3 h. Subsequently, the 2M HCl solution was used to remove the metal ions and residual KOH. After the as-prepared simple was washed with deionized water to neutrality, the target product WSCPC was obtained. For convenient comparison, we named the samples WSCPC-0, WSCPC-1, WSCPC-2, WSCPC-3, WSCPC-4 and WSCPC-5 (the number represents the mass ratio of activator to carbon). The preparation process of WSCPC is shown in Fig. 2. Materials and reagents are shown in Table SI of the supplementary materials.

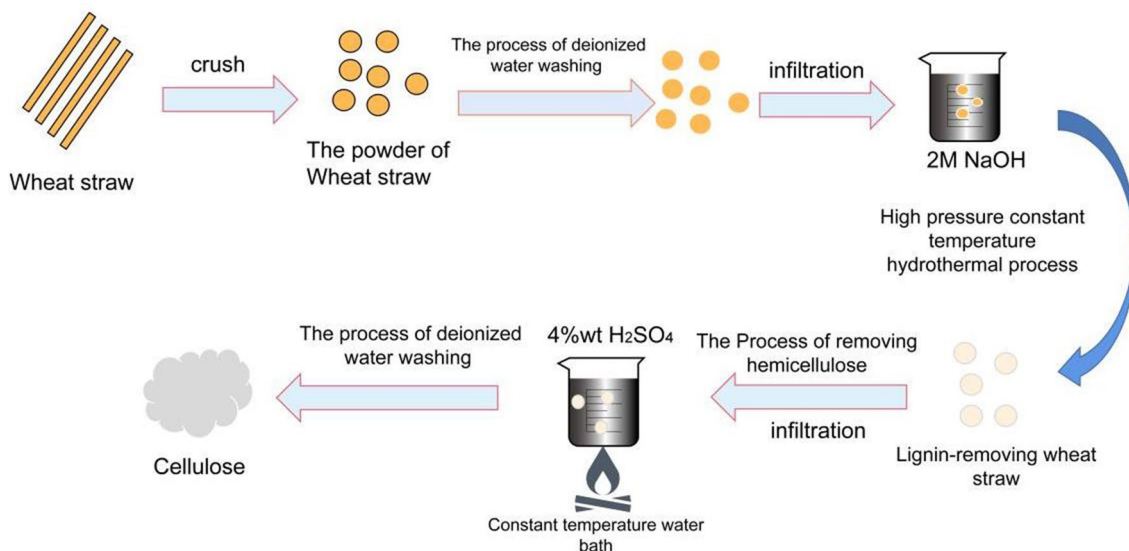


Fig. 1 Illustration of preparation process of wheat straw cellulose.

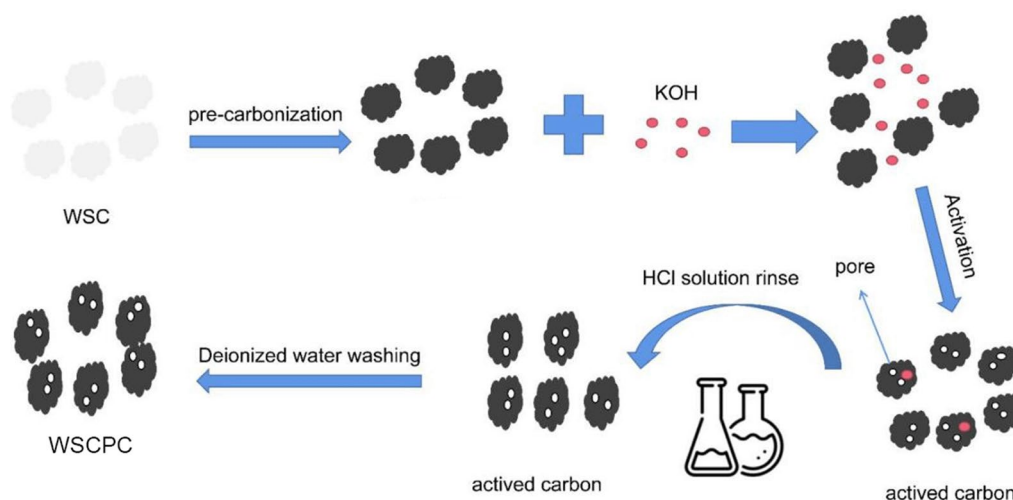


Fig. 2 Preparation process of WSCPC.

Characterization of Materials

Physicochemical characterization. X-ray diffraction (XRD, Rigaku) with Cu-K α radiation and Raman spectroscopy (Jobin Yvon T6400, 514 nm) were employed to measure the crystal structure of the as-obtained materials. The morphology and structure of WSCPC were characterized by scanning electron microscopy (SEM, JEOL-JSM-6700F, JEOL Ltd, Tokyo, Japan) and transmission electron microscopy (TEM, JEM-2100F, JEOL Ltd, Tokyo, Japan). The specific surface area and pore size were analyzed using the nitrogen adsorption-desorption test (Micromeritics, ASAP2420, Micromeritics Instrument, Norcross, GA, USA).

Electrochemical test. Electrochemical characteristics were measured by CR2025 button-type lithium-ion batteries. The working electrode, carbon black (Super-p), and polyvinylidene fluoride (PVDF) were dispersed in *N*-methyl-2-pyrrolidone (NMP) solvent at a mass ratio of 8:1:1 to form a uniform slurry. The as-obtained slurry was coated on Cu foil and dried in a vacuum drying oven at 120°C for 8 h. Then, the Cu foil was stamped into discs with a diameter of 11mm, and the mass loading of active material was about 2 mg cm⁻². For the electrolyte, ethylene carbonate (EC):dimethyl carbonate (DMC) = 1:1 (volume ratio) was used as the organic solvent and 1 mol L⁻¹ of LiPF₆ as the solute. Batteries were assembled in a glove box filled with

Ar atmosphere. We used the CT2001A lithium-ion battery test system to test the batteries from 0.1 V to 3 V at room temperature. A CH1604E electrochemical workstation was used to perform cyclic voltammetry (CV) testing at room temperature, with a scan rate of 0.5 mV s^{-1} between 0.1 V and 3 V. The same instrument was also used in electrochemical impedance spectroscopy (EIS) analysis, which was measured with an AC voltage of 5 mV in the frequency range of 0.1 Hz to 100 kHz.

Results and Discussion

Characterization of WSCPC

The crystal structure of WSCPC was confirmed by the XRD pattern, as shown in Fig. 3a. The samples show two diffraction peaks near 22° and 45° , which are the (002) and (100) typical crystal planes of amorphous carbon. The broad

peak of (002) is usually related to the interlayer structure of multiple graphene sheets, and the weak diffraction peak of the (100) crystal plane is indicative of the existence of sp^2 hybridized hexagonal structure.³⁸ Figure 3b shows the result of Raman spectra. A peak at $\sim 1340 \text{ cm}^{-1}$ points to the D-band (related to defective graphite structure) and a peak at $\sim 1600 \text{ cm}^{-1}$ points to the G-band (related to sp^2 hybrid carbon). Through the analysis of the Raman results, I_D/I_G values (intensity ratio of the D-band peak to G-band peak) of WSCPC-0, WSCPC-1, WSCPC-2, WSCPC-3, WSCPC-4, and WSCPC-5 are 2.18, 2.84, 2.96, 3.08, 3.41, and 2.71, respectively. The samples all have abundant active sites and pore structures. Obviously, WSCPC-4 has the highest I_D/I_G value, which suggests that the material contains the richest defects and the highest degree of disorder. These defects are beneficial for Li^+ insertion into the anode electrode material to improve the electrochemical activity.

The Brunauer-Emmett-Teller (BET) curves and pore size distribution of the WSCPC are shown in Fig. 4. It is

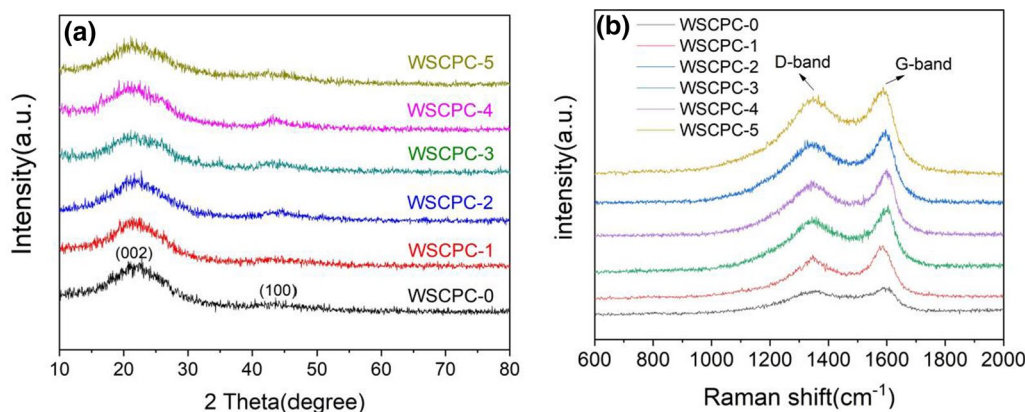


Fig. 3 (a) XRD pattern and (b) Raman spectra of WSCPC.

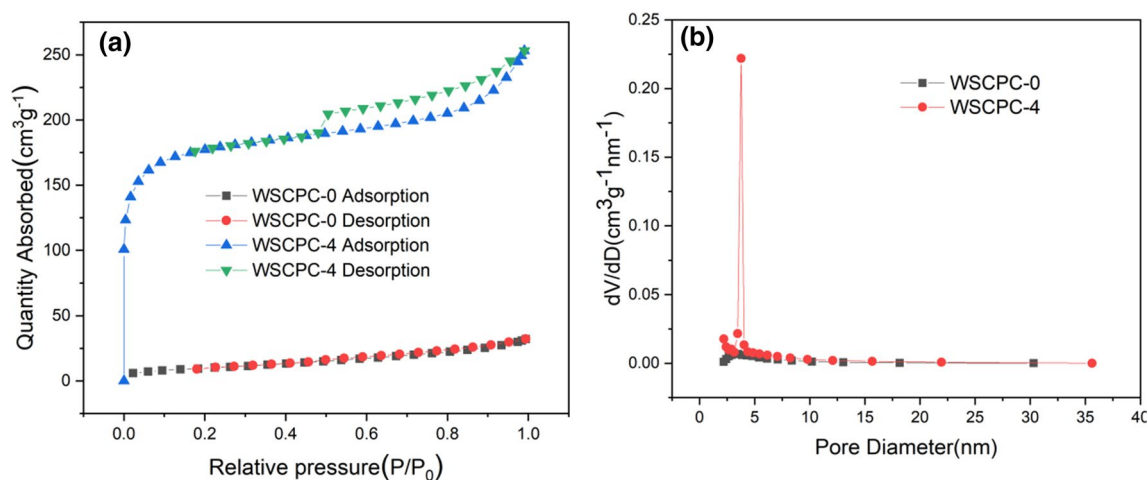


Fig. 4 (a) Nitrogen adsorption-desorption isotherms and (b) Pore size distribution of WSCPC-0 and WSCPC-4.

displayed that the specific surface areas of the WSCPC-0 and WSCPC-4 are 161 and 628 $\text{m}^2 \text{g}^{-1}$, respectively. WSCPC-4 shows a total pore volume of 0.172 $\text{cm}^3 \text{g}^{-1}$ compared to WSCPC-0 of 0.053 $\text{cm}^3 \text{g}^{-1}$. As shown in supplementary Figure S1, the specific surface areas of WSCPC-1, WSCPC-2, WSCPC-3, and WSCPC-5 are 239, 380, 563, and 253 $\text{m}^2 \text{g}^{-1}$, respectively. The total pore volume of the four samples is 0.078, 0.083, 0.091, and 0.075 $\text{cm}^3 \text{g}^{-1}$. As the weight of activators increases, meso/micropores are formed due to the influence of the activator, causing defects and a pore structure on the surface of the material. Simultaneously, specific surface area and pore volume gradually increase. Obviously, the specific surface area and porosity of WSCPC-4 show encouraging results compared to other samples. However, as the amount of KOH continues to increase, the value showed a decrease. It is attributed to excessive activator destroying the pore structure of the sample and making the internal structure unstable. From Table I, it is observed that the concentration of KOH is important in adjusting the overall porosity of WSCPC. For the adsorption-desorption isotherms of WSCPC-4, when the relative pressure is low ($P/P_0 < 0.01$), the adsorption increases sharply as the relative pressure increases. This indicates the presence of micropores in the sample. When the relative pressure is close to 1, the adsorption curve has a slight rising slope, indicating the presence of macropores. In addition, when the relative pressure is $P/P_0 > 0.6$, an obvious hysteresis loop begins to appear. The appearance of the hysteresis ring confirms that there are rich mesopores. The shape of the isothermal desorption curve can be expressed as type IV. The pore size distribution is shown in Fig. 4b. The higher mesoporous content of WSCPC-4 can be seen as a nice advantage for the rapid transport of electrolyte ions, which is beneficial to increasing the reaction rate in the electrochemistry reaction process and generating a larger discharge specific capacity. The synergistic effect of micropores, mesopores, and macropores promotes the penetration of electrolytes, improves the surface utilization of electrode materials, and provides a path with lower internal resistance for the transmission of Li^+ and electrons.

Table I Physical parameters of WSCPC

Sample	S_{BET} ($\text{m}^2 \text{g}^{-1}$)	Pore volume ($\text{cm}^3 \text{g}^{-1}$)
WSCPC-0	161	0.053
WSCPC-1	239	0.078
WSCPC-2	380	0.083
WSCPC-3	563	0.091
WSCPC-4	628	0.172
WSCPC-5	253	0.075

For more details on WSCPC, we adopted scanning electron microscopy to characterize the microstructure of the samples. As shown in Fig. 5, the microstructure of the WSCPC-0 sample is smooth and block-like at about 2 μm . It was found that the surface of WSCPC-1 became rough with slight traces of activation. From the SEM image of WSCPC-2, there are pores of different sizes in the carbon, which are formed by calcination at high temperatures. When the ratio of KOH is increased to 3:1 and 4:1, the pore structure of the sample becomes more abundant and obvious surface defects appear. It can be observed that WSCPC-4 has a massive morphology with large pores. These pores and defects are beneficial to the diffusion of lithium ions in the electrode/electrolyte interface, and macropores can serve as an ion buffer layer. But when the KOH ratio increased to 5:1, the pore structure began to collapse and the carbon matrix broke. This is because an excessively high proportion of activators at high temperatures will destroy the porous structure formed by catalysis and oxidation.

The clear morphology of WSCPC is shown in Fig. 6 and Figure S2 (see supplementary file), which was analyzed using TEM. It can be seen from supplementary Figure S2 that WSCPC-0 is a micron-level smooth carbon matrix with few pore structures. On the surface of WSCPC-1 and WSCPC-2, the pore structure gradually appeared, which is consistent with the results obtained from the SEM image. Figure 6 shows the TEM images of WSCPC-3, WSCPC-4, and WSCPC-5. Obviously, as the amount of KOH increases, the pore structure of the carbon block increases. Especially when the ratio reaches 4:1, a wealth of micropores and mesopores are discovered on the surface (Fig. 6c and d). This not only shortens the length of ion transmission and diffusion but also increases the contact area between the electrode and the electrolyte. Nevertheless, as the pore size of WSCPC-5 becomes larger, the carbon block becomes smaller, and the surface begins to collapse, which leads to a decrease in the activation effect of KOH.

Electrochemical Performance

Figure 7a and b are the CV curves of the WSCPC-0 and WSCPC-4 in the first three charge and discharge cycles. The CV curves of other samples are shown in supplementary Figure S3. The reduction peak area of the initial cycle of the sample is significantly larger than the reduction peak areas of the second and third cycles. This difference is due to electrolyte decomposition and irreversible capture of Li^+ in the carbon matrix. During the negative scanning, the reduction peak can be observed around 1.75 V, but it disappears in the next two cycles. This phenomenon occurs because of the irreversible reaction between the surface of the carbon material during the discharge process in the first cycle. In addition, a chemical reaction occurred between the interface

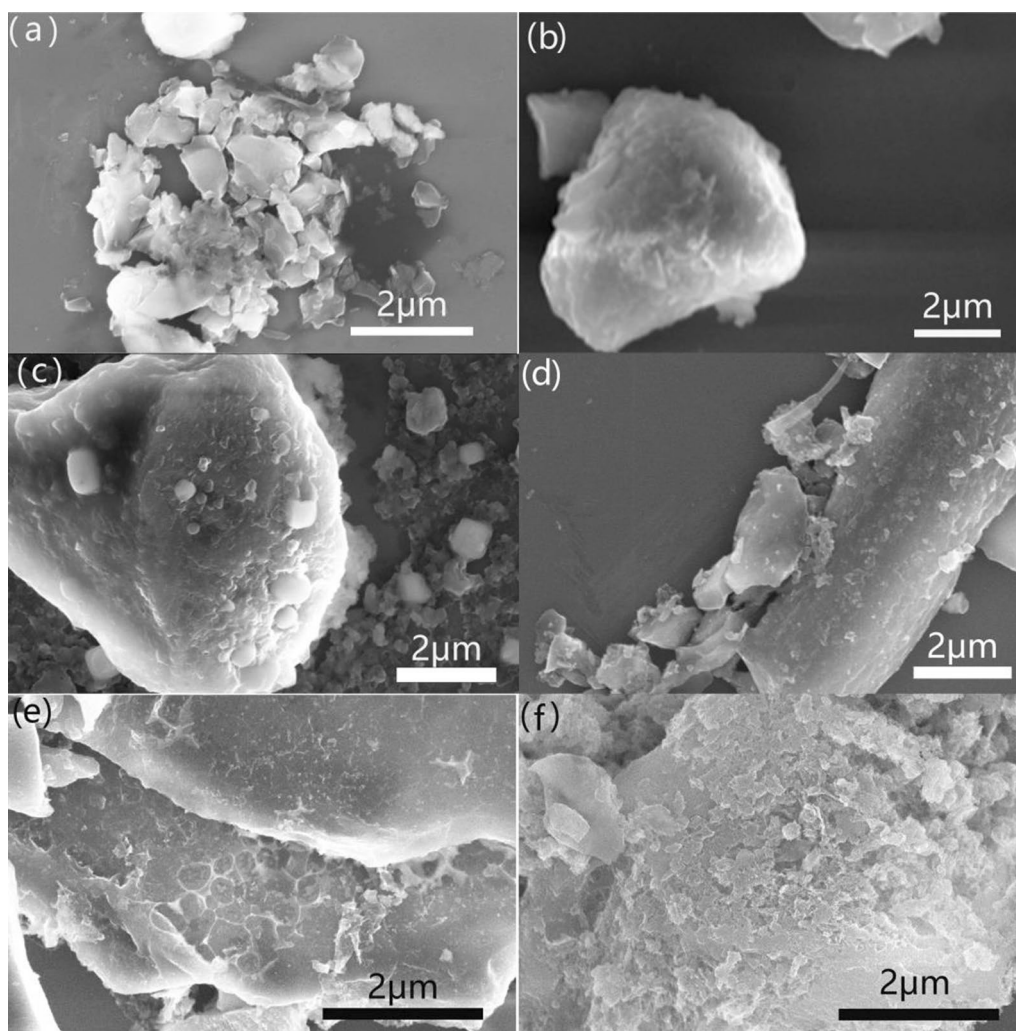


Fig. 5 The SEM images of (a) WSCPC-0 (b) WSCPC-1 (c) WSCPC-2 (d) WSCPC-3 (e) WSCPC-4 and (f) WSCPC-5.

of the electrode/electrolyte to form a solid electrolyte interphase layer (SEI) film, and a separate reduction peak appears at about 0.65 V.³⁹ During the positive scanning, a relatively flat oxidation peak appears between 0 V and 0.5 V, which is caused by the extraction of Li^+ from the micropores or vacancies of the carbon material. Figure 7c and d and Figure S4 show the charge and discharge characteristic curves of the samples in the 1st, 2nd, 50th and 100th cycles at a current rate of 0.2 C. The charge curve shows two plateaus near 0.25 V and 1.1 V, which corresponds to the potential position of the oxidation peak in the CV curve. In addition, it can be seen from the figure that the specific capacity of the samples after KOH activation has been significantly improved. The initial specific discharge capacities of WSCPC-0, WSCPC-1, WSCPC-2, WSCPC-3, WSCPC-4, and WSCPC-5 are 1075, 1372, 1770, 1894, 2750, and 2384 mAh g^{-1} , respectively. However, the samples have a lower Coulomb efficiency, which is determined by the structural features of the carbon

material. The charge and discharge curves of the 50th cycle and 100th cycle of these samples overlap very well, indicating that the electrochemical performance has stabilized.

Figure 8 shows the electrochemical cycling performance of the samples at 0.2 C. The discharge capacity of the samples stabilized at 425.3, 506.7, 699.8, 799.8, 1420.5, and 1049 mAh g^{-1} after a large number of charge and discharge cycles. With the increase in the proportion of KOH impregnation, the activated porous carbon material significantly increases in both the initial specific capacity and the stable discharge specific capacity after cycling at a rate of 0.2 C. However, when the ratio of KOH reaches 5:1, the electrochemical performance tends to decrease, indicating that an appropriate amount of KOH as a strong oxidant can effectively improve the electrochemical performance.

Figure 9 shows the rate performance of the WSCPC. It can be seen that the carbon material after KOH activation has been significantly improved, and the WSCPC-4 material

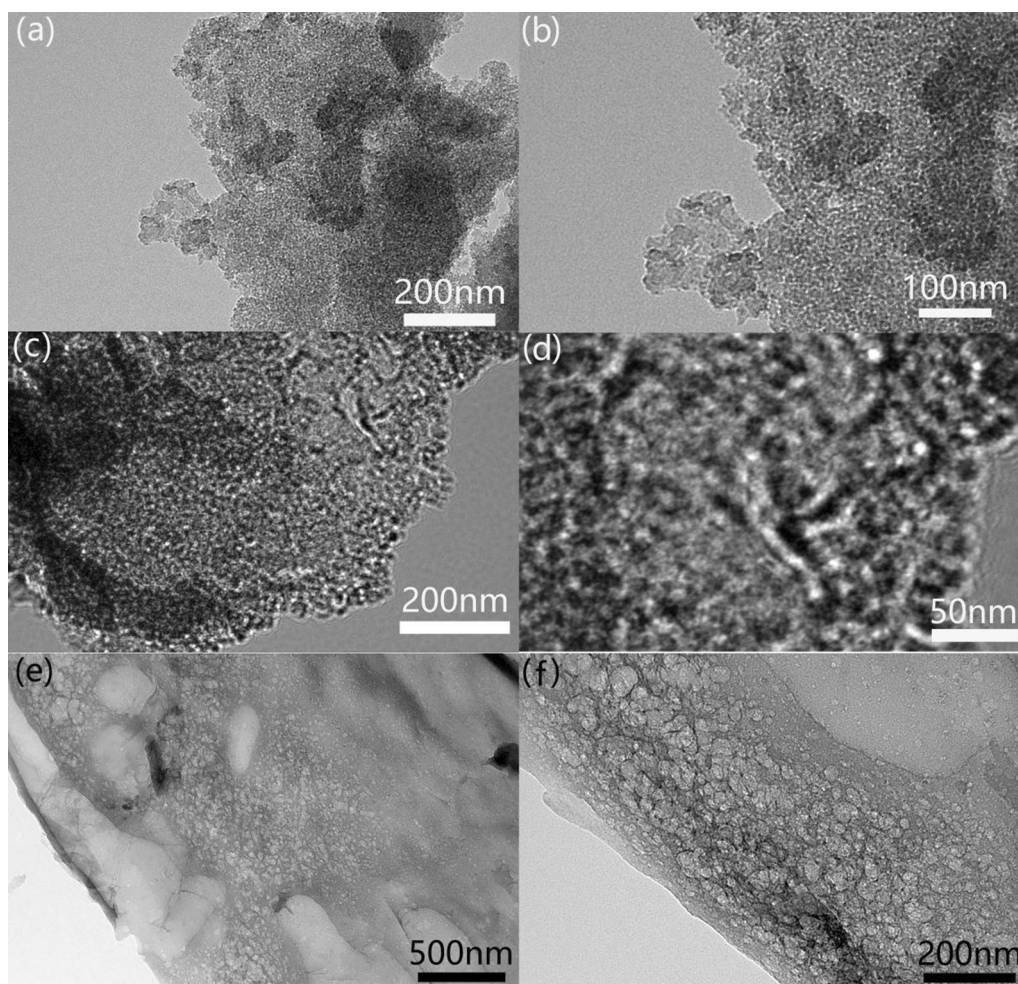


Fig. 6 The TEM images of (a, b) WSCPC-3 (c, d) WSCPC-4 (e, f) WSCPC-5.

with the richest mesoporous structure has the best variable current rate performance. When the current intensity is 0.2 C, 0.5 C, 1 C, 2 C, 5 C, the corresponding discharge specific capacities are 1355, 1155, 1025, 925, 810 mAh g⁻¹, respectively. With the WSCPC-4 returns to 0.2 C after the variable rate charge and discharge test, its specific discharge capacity can still be restored to 1300 mAhg⁻¹, indicating that it has good cycle stability. However, the rate performance of WSCPC-0 under the same test environment is only 480, 375, 290, 215, 165, and 445 mAh g⁻¹, respectively. In addition, the rate performance of WSCPC-5 is worse than that of WSCPC-4, indicating that excessive KOH cannot continue to increase its reversible capacity.

Figure 10a shows the Nyquist impedance spectroscopy of the samples. It can be seen that the charge transfer resistance of the WSCPC-4 in the high-frequency region is significantly less than that of other samples. This is because the abundant mesopore distribution in WSCPC-4 makes it easier for the electrolyte to react with the surface of the carbon material and accelerates the insertion and deintercalation of

lithium ions during the charge and discharge process of the material, making the charge transfer easier.⁴⁰ The slope of the straight-line part of WSCPC-4 at the middle and low-frequency positions is high, which indicates that the diffusion resistance of lithium ions has been significantly improved. Figure 10b shows the impedance curves of the WSCPC-4 sample before and after 100 cycles. The diameter of the semicircle in the high-frequency zone of the uncycled WSCPC-4 is significantly larger than the semicircle diameter after the cycles, indicating that the interface charge transfer resistance of WSCPC-4 decreases after a certain charge and discharge cycle. This is because it is easier for lithium ions to enter/exit the electrode during the charge-discharge process. Figure 10c shows the equivalent circuit simulation model of WSCPC. The resistance R_e represents the resistance of the material, the resistance R_{ct} and the capacitance C_{pe} , respectively, represent the charge transfer resistance and electric double-layer capacitance of the lithium-ion batteries, and Z_w represents the Warburg impedance related to lithium-ion diffusion during the charging and discharging process of the

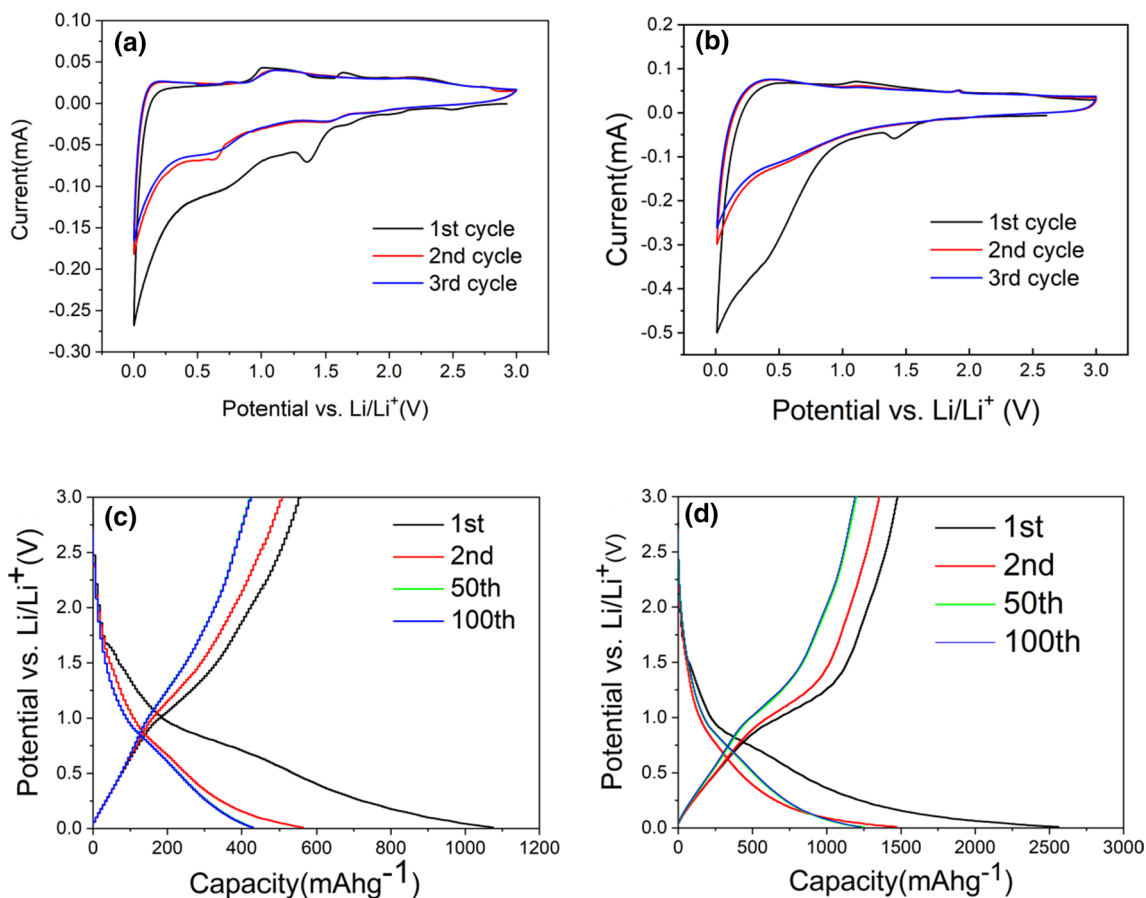


Fig. 7 CV curves of (a) WSCPC-0 (b) WSCPC-4, and Charge/discharge curves of (c) WSCPC-0 (d) WSCPC-4.

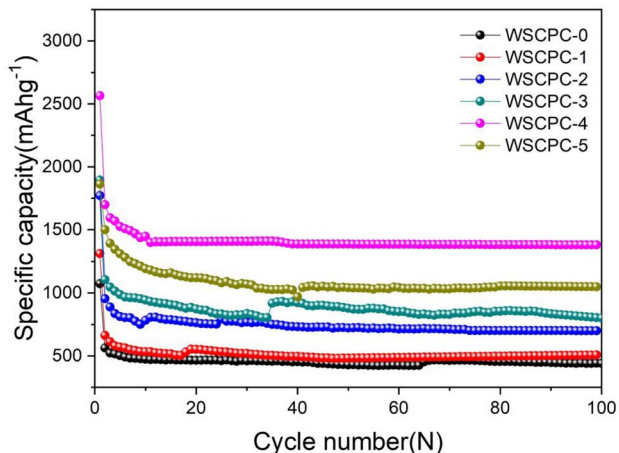


Fig. 8 Cycling performance at 0.2 C of WSCPC-0, WSCPC-1, WSCPC-2, WSCPC-3, WSCPC-4, and WSCPC-5.

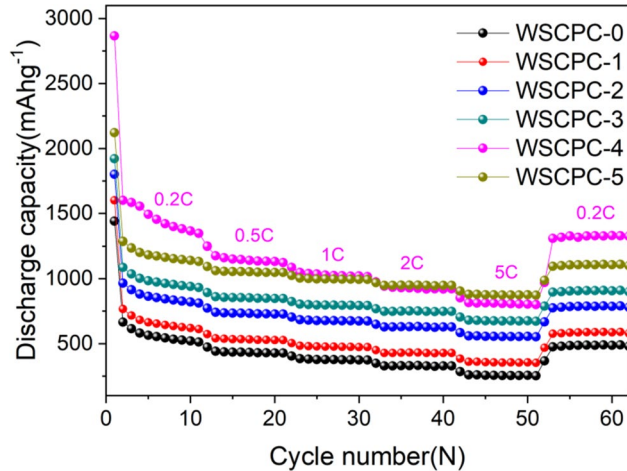


Fig. 9 The rate performance of WSCPC-0, WSCPC-1, WSCPC-2, WSCPC-3, WSCPC-4, and WSCPC-5.

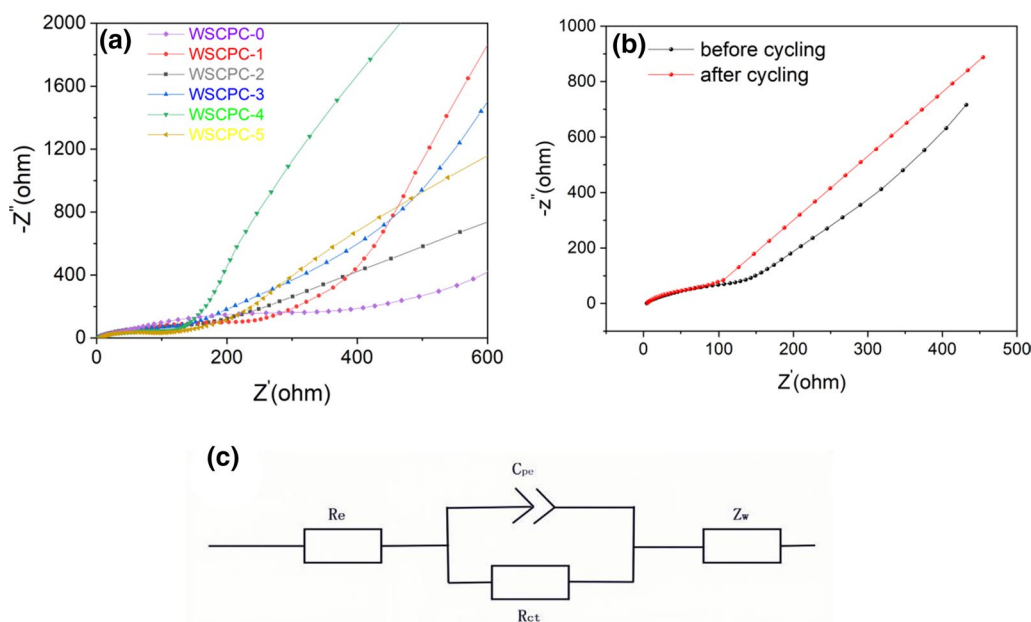


Fig. 10 (a) The impedance curves of before cycling of WSCPC (b) The impedance curves of before and after cycling of WSCPC-4 and (c) the equivalent circuit simulation model of WSCPC.

lithium-ion batteries. After simulation calculation, the R_{ct} values of the WSCPC-0, WSCPC-1, WSCPC-2, WSCPC-3, WSCPC-4 and WSCPC-5 samples are 550 Ω , 418 Ω , 325.2 Ω , 265 Ω , 172 Ω and 202.5 Ω , respectively. Through simulation calculation, it can be found that the charge transfer resistance of WSCPC-4 is the lowest, which proves that the material has the best electrical conductivity.

Conclusion

In conclusion, the application of wheat straw-based activated carbon to the anode electrode of lithium-ion batteries provides an uncomplicated method for the industrial production of low-cost, high-capacity wheat straw-based anode electrode materials. The carbon material derived from wheat straw obtained by carbonization and activation is a typical amorphous carbon. Among the samples tested, the activation effect of WSCPC-4 is superior. It has the most obvious pore structure, and the BET surface area reaches 628 $\text{m}^2 \text{g}^{-1}$. After 100 cycles at 0.2 C, WSCPC-4 can achieve a high reversible stable capacity of 1420 mAh g^{-1} . Compared with an unactivated sample, the electrochemical performance of activated carbon has been significantly improved. The activation theory provides an effective method for the rapid and low-cost preparation of anode electrode materials and the comprehensive utilization of wheat straw.

Supplementary Information The online version contains supplementary material available at <https://doi.org/10.1007/s11664-021-09173-3>.

Acknowledgments This work was financially supported by the Jilin Provincial Scientific and Technological Department (20190302055GX, YDZJ202101ZYTS145) and the China Postdoctoral Science Foundation (2017M611321).

Conflict of interest The authors declare that they have no conflict of interest.

References

1. L. Lu, X. Han, J. Li, J. Hua, and M. Ouyang, *J. Power Sources* 226, 272 (2013).
2. B. Scrosati, J. Hassoun, and Y. Sun, *Energy Environ. Sci.* 4, 3287 (2011).
3. J.M. Tarascon, and M. Armand, *Nature* 414, 359 (2001).
4. V. Singh, D. Joung, L. Zhai, S. Das, S.I. Khondaker, and S. Seal, *Prog. Mater. Sci.* 56, 1178 (2011).
5. X. Huang, X. Qi, F. Boey, and H. Zhang, *Chem. Soc. Rev.* 41, 666 (2012).
6. C. Wang, L. Cao, J. Huang, J. Li, and K. Kajiyoshi, *Renew. Sustain. Energy Rev.* 138, 110564 (2020).
7. Y. Sun, Q. Wu, and G. Shi, *Energy Environ. Sci.* 4, 1113 (2011).
8. S. Han, D. Jung, J. Jeong, and E.S. Oh, *Chem. Eng. J.* 254, 597 (2014).
9. C. Hernandez-Rentero, V. Marangon, M. Olivares-Marin, V. Gomez-Serrano, A. Caballero, J. Morales, and J. Hassoun, *J. Colloid Interface Sci.* 573, 396 (2020).
10. Y. Liu, J. Chen, B. Cui, P. Yin, and C. Zhang, *J. Carbon Res.* 4, 53 (2018).

11. W. Long, B. Fang, A. Ignaszak, Z. Wu, Y. Wang, and D. Wilkinson, *Chem. Soc. Rev.* 46, 7176 (2017).
12. T. Yokokura, J. Rodriguez, and V. Pol, *ACS Omega* 5, 19715 (2020).
13. M. Zulfajri, H. Abdelhamid, S. Sudewi, S. Dayalan, A. Rasool, A. Habib, and G. Huang, *Biosensors* 10, 68 (2020).
14. V. Rimal, S. Shishodia, P. Srivastava, S. Gupta, and A. Mallick, *Appl. Nanosci.* 11, 1225 (2021).
15. J. Zhu, J. Roscow, S. Chandrasekaran, L. Deng, P. Zhang, T. He, K. Wang, and L. Huang, *Chemsuschem* 13, 1275 (2020).
16. W. Tang, Y. Zhang, Y. Zhong, T. Shen, X. Wang, X. Xia, and J. Tu, *Mater. Res. Bull.* 88, 234 (2017).
17. Z. Bi, Q. Kong, Y. Cao, G. Sun, F. Su, X. Wei, X. Li, A. Ahmad, L. Xie, and C. Chen, *J. Mater. Chem. A* 7, 16028 (2019).
18. H. Yuan, T. Liu, Y. Liu, J. Nai, Y. Wang, W. Zhang, and X. Tao, *Chem. Sci.* 10, 7484 (2019).
19. J. Deng, M. Li, and Y. Wang, *Green Chem.* 18, 4824 (2016).
20. Y. Sun, J. Xue, S. Dong, Y. Zhang, Y. An, B. Ding, T. Zhang, H. Dou, and X. Zhang, *J. Mater. Sci.* 55, 5166 (2020).
21. S. Natarajan, Y. Lee, and V. Aravindan, *Chem. Asian J.* 14, 936 (2019).
22. T. Liu, and X. Li, *Mater. Technol.* 34, 232 (2019).
23. H. Hou, X. Qiu, W. Wei, Y. Zhang, and X. Ji, *Adv. Energy Mater.* 7, 1602898 (2017).
24. T. Liu, R. Kavian, Z. Chen, S. Cruz, S. Noda, and S. Lee, *Nanoscale* 8, 3671 (2016).
25. M. Chen, C. Yu, S. Liu, X. Fan, C. Zhao, X. Zhang, and J. Qiu, *Nanoscale* 7, 1791 (2015).
26. H. Liu, X. Liu, W. Li, X. Guo, Y. Wang, G. Wang, and D. Zhao, *Adv. Energy Mater.* 7, 1700283 (2017).
27. Z. Zhao, S. Das, G. Xing, P. Fayon, P. Heasman, M. Jay, S. Bailey, C. Lambert, H. Yamada, T. Wakihara, A. Trewin, T. Ben, S. Qiu, and V. Valtchev, *Angew. Chem.-Int. Ed.* 57, 11952 (2018).
28. K. Yu, J. Wang, X. Wang, J. Liang, and C. Liang, *Mater. Chem. Phys.* 243, 122644 (2020).
29. V. Subramanian, C. Luo, A.M. Stephan, K.S. Nahm, S. Thomas, and B. Wei, *J. Phys. Chem. C* 111, 7527 (2007).
30. J. Hou, C. Cao, F. Idrees, and X. Ma, *ACS Nano* 9, 2556 (2015).
31. S. Sekar, Y. Lee, D. Kim, and S. Lee, *Nanomaterials* 9, 871 (2019).
32. C. Gao, W. Xiao, G. Ji, Y. Zhang, Y. Cao, and L. Han, *Bioresour. Technol.* 241, 214 (2017).
33. S. Zhu, W. Huang, W. Huang, K. Wang, Q. Chen, and Y. Wu, *Bioresour. Technol.* 185, 234 (2015).
34. L. Chen, Y. Zhang, C. Lin, W. Yang, Y. Meng, Y. Guo, M. Li, and D. Xiao, *J. Mater. Chem. A* 2, 9684 (2014).
35. X. Zhou, F. Chen, T. Bai, B. Long, Q. Liao, Y. Ren, and J. Yang, *Green Chem.* 18, 2078 (2016).
36. F. Chen, L. Ma, J. Ren, M. Zhang, X. Luo, B. Li, Z. Song, and X. Zhou, *Materials* 11, 989 (2018).
37. H. Wan, and X. Hu, *Chem. Phys.* 521, 108 (2019).
38. R. Li, J. Huang, J. Ren, L. Cao, J. Li, B. Li, G. Lu, and A. Yu, *J. Alloys Compd.* 818, 152849 (2019).
39. F. Yuen, and B.H. Hameed, *Adv. Colloid Interface Sci.* 149, 19 (2008).
40. W. Fan, H. Zhang, H. Wang, X. Zhao, S. Sun, J. Shi, M. Huang, W. Liu, Y. Zheng, and P. Li, *Rsc Adv.* 9, 32382 (2019).

Publisher's Note Springer Nature remains neutral with regard to jurisdictional claims in published maps and institutional affiliations.